Supplementary Information

Transition metal vacancy and position engineering enables reversible anionic redox reaction for sodium storage

Congcong Cai[1,5], Xinyuan Li[1,5], Jiantao Li[2,5,*], Ruohan Yu[1,5], Ping Hu[1], Ting Zhu[1], Tianyi Li[3], Sungsik Lee[3], Nuo Xu[1], Hao Fan[1], Jinsong Wu[1], Liang Zhou[1,*], Liqiang Mai[1,*], Khalil Amine[2,4*]

[1]State Key Laboratory of Advanced Technology for Materials Synthesis and Processing, Wuhan University of Technology, Wuhan 430070, China

[2]Chemical Sciences and Engineering Division, Argonne National Laboratory, Lemont, Illinois 60439, USA

[3]X-ray Science Division, Advanced Photon Source, Argonne National Laboratory, Lemont, Illinois 60439, USA

[4]Pritzker School of Molecular Engineering, The University of Chicago, Chicago, IL 60637, USA

[5]These authors contributed equally to this work.

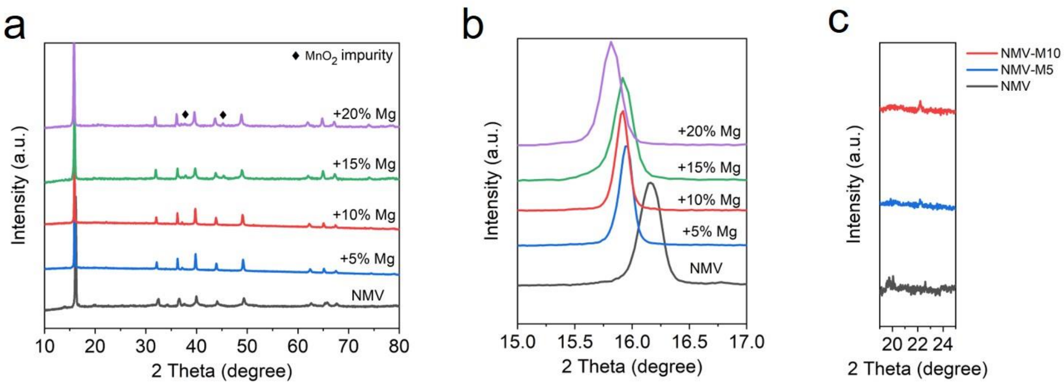

Supplementary Figure 1. (a) XRD patterns of the samples with different Mg contents; Enlarged XRD patterns at (a) 15–17^{o} with increasing Mg contents and (b) 19–25^{o} of NMV, NMV-M5, and NMV-M10.

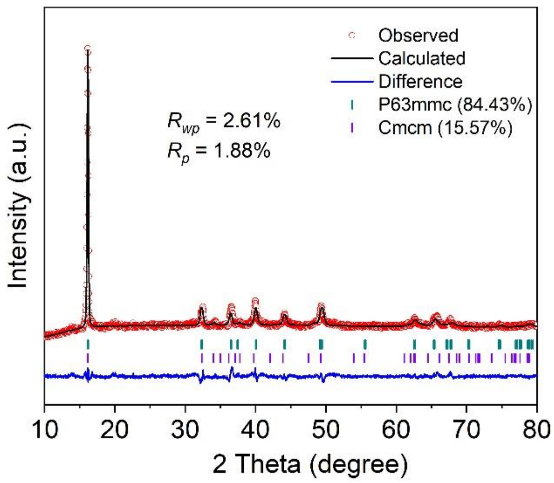

Supplementary Figure 2. XRD Rietveld refinement pattern of NMV.

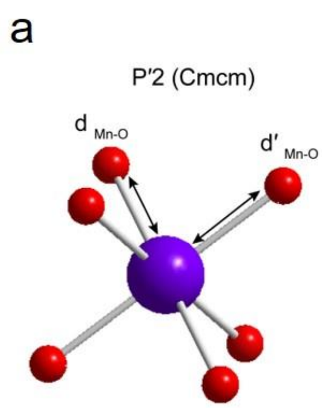

Supplementary Figure 3. Schematic illustration of MnO_6 octahedra of (a) P′2 and (b) P2 phases.

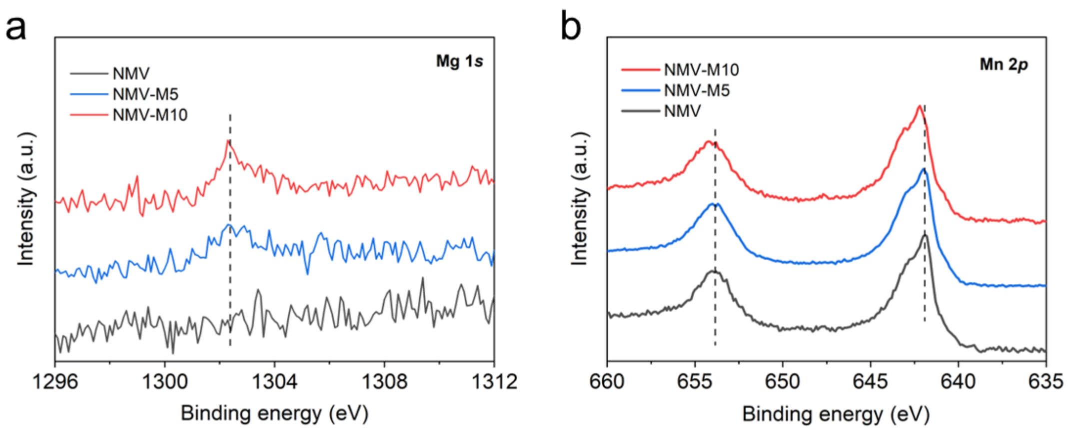

Supplementary Figure 4. (a) Mg 1*s* and (b) Mn 2*p* XPS spectra of NMV, NMV-M5, and NMV-M10.

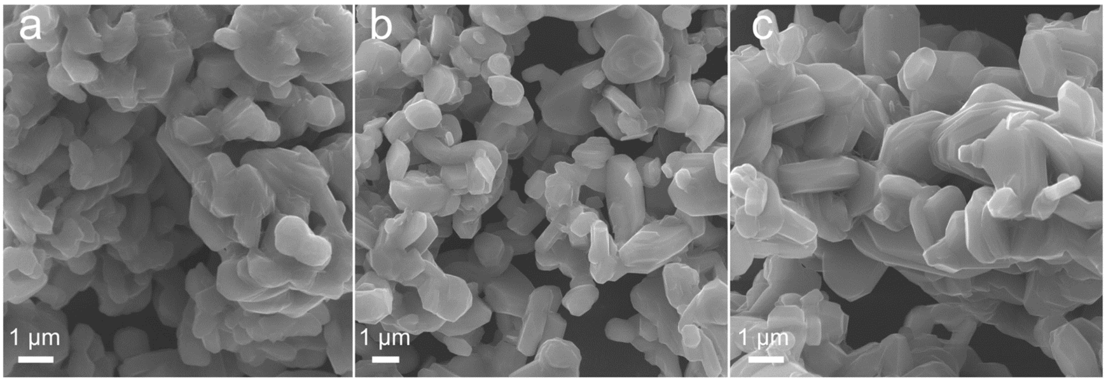

Supplementary Figure 5. SEM images of (a) NMV, (b) NMV-M5, and (c) NMV-M10.

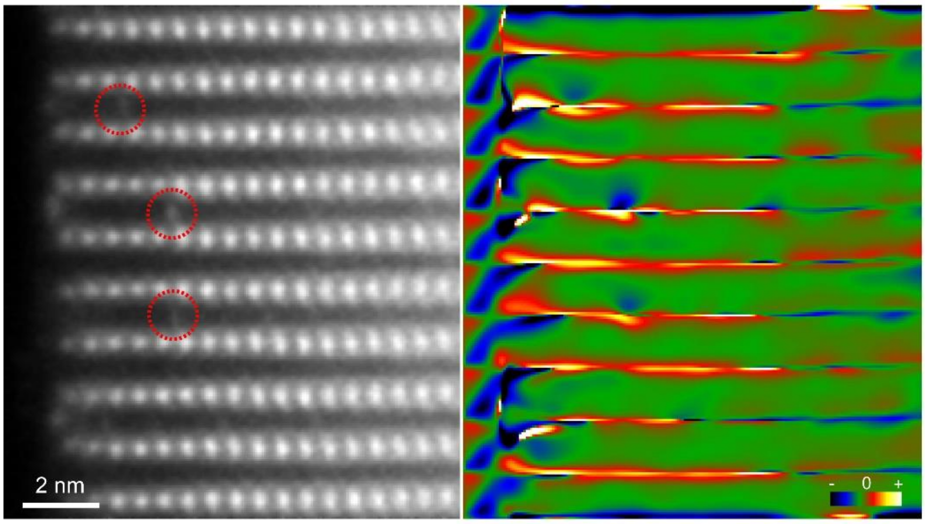

Supplementary Figure 6. GPA analysis based on HAADF-STEM of NMV-M10.

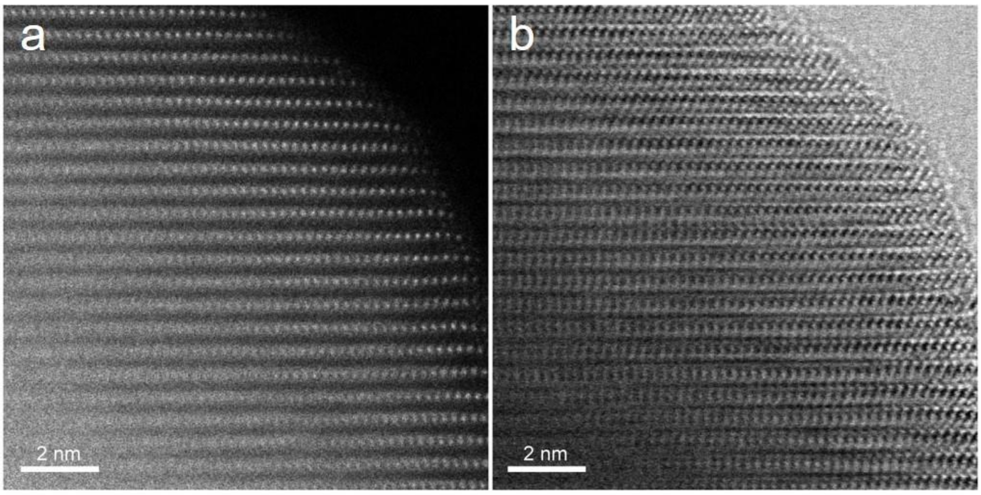

Supplementary Figure 7. (a) HAADF- and (b) ABF- STEM images of NMV.

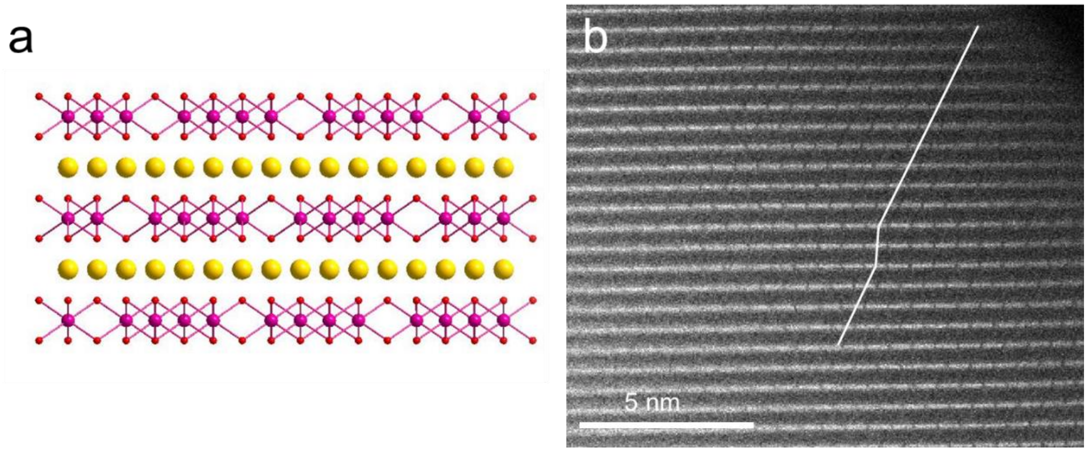

Supplementary Figure 8. (a) Schematic illustration of the existence of vacancies in TM layer; (b) HAADF image of NMV where ribbon-ordered TM vacancies can be observed.

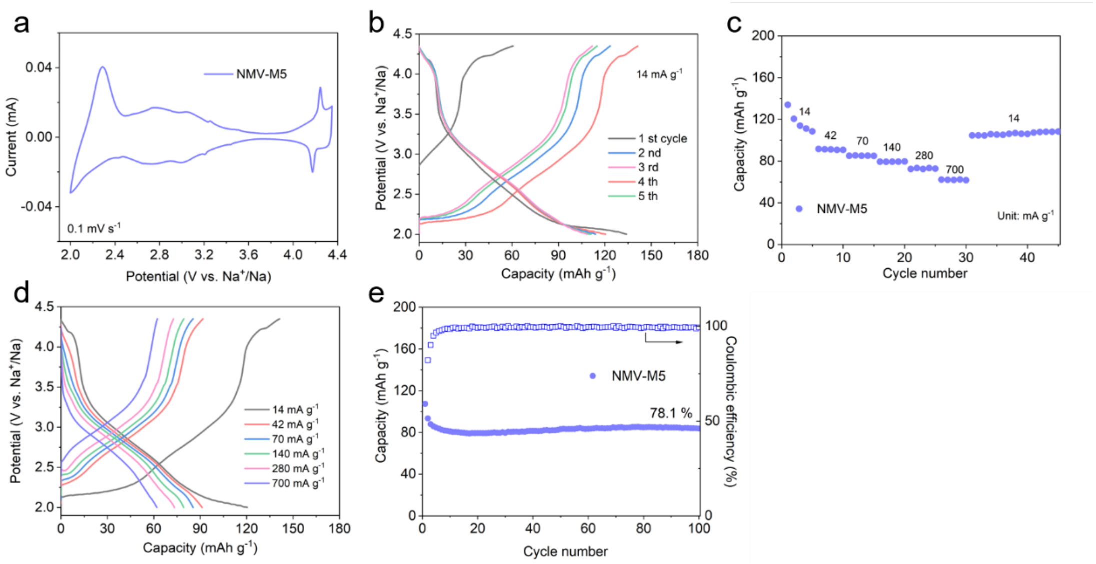

Supplementary Figure 9. Electrochemical performances of NMV-M5. (a) CV curve at 0.1 mV s^{-1}; (b) first five charge/discharge profiles at 14 mA g^{-1}; (c) rate performance; (d) GCD profiles of the second cycle at different current densities; (e) the cycling performance and Coulombic efficiencies at 42 mA g^{-1}.

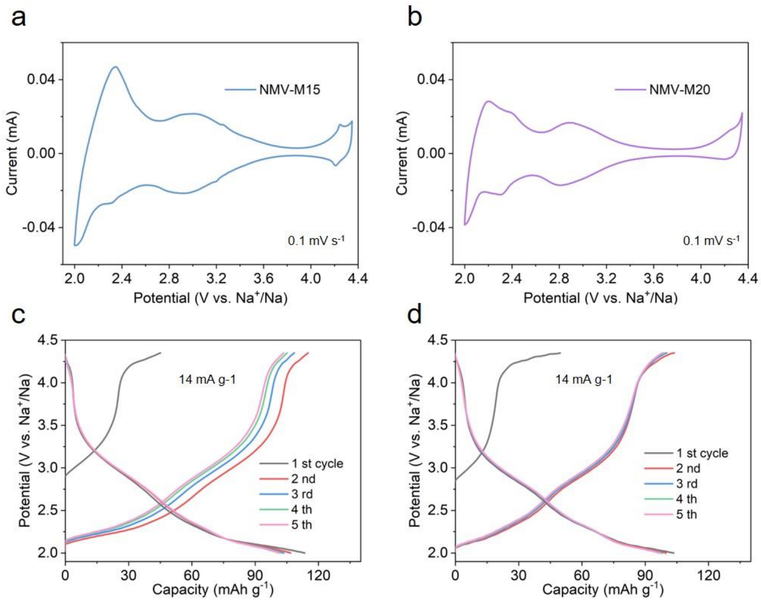

Supplementary Figure 10. Electrochemical performances of NMV-M15 and NMV-M20. CV curves of (a) NMV-M15 and (b) NMV-M20; the first five charge/discharge profiles of (c) NMV-M15 and (d) NMV-M20 at 14 mA g^{-1}.

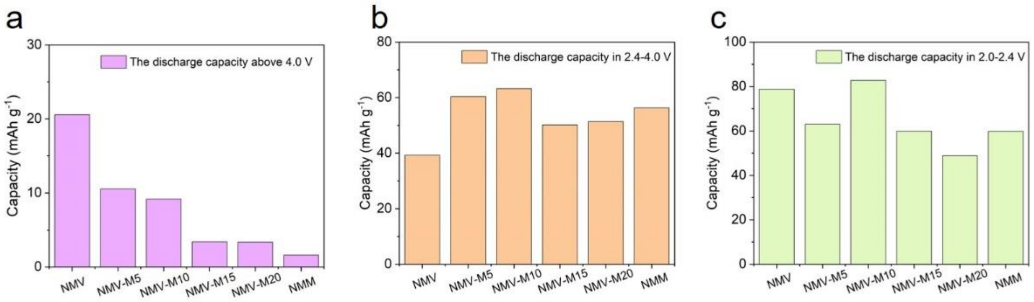

Supplementary Figure 11. The discharge capacity contributions of the samples from (a) above 4.0 V, (b) 2.4–4.0 V, and (c) 2.0–2.4 V at 14 mA g^{-1}.

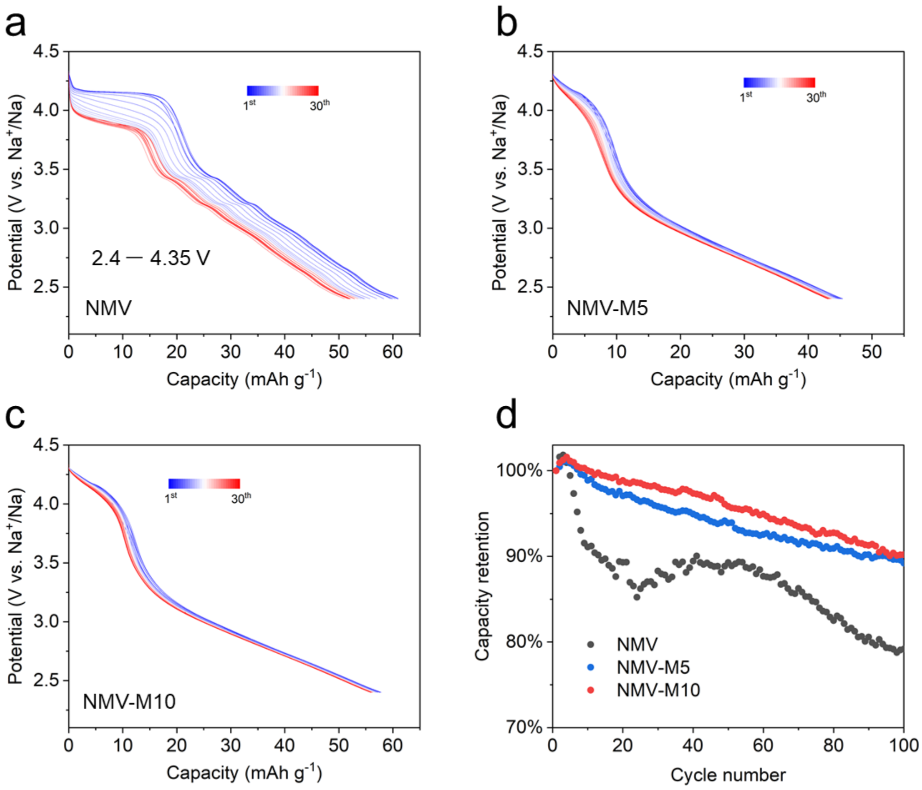

Supplementary Figure 12. Cycle tests in the potential range of 2.4–4.35 V to exclude the influence of cationic redox (Mn^{3+}/Mn^{4+}). The discharge profiles of (a) NMV, (b) NMV-M5, and (c) NMV-M10 at first 30 cycles, which were tested at 42 mA g^{-1} within 2.40–4.35 V; (d) the cycling performances of NMV, NMV-M5, and NMV-M10 within 2.40–4.35 V.

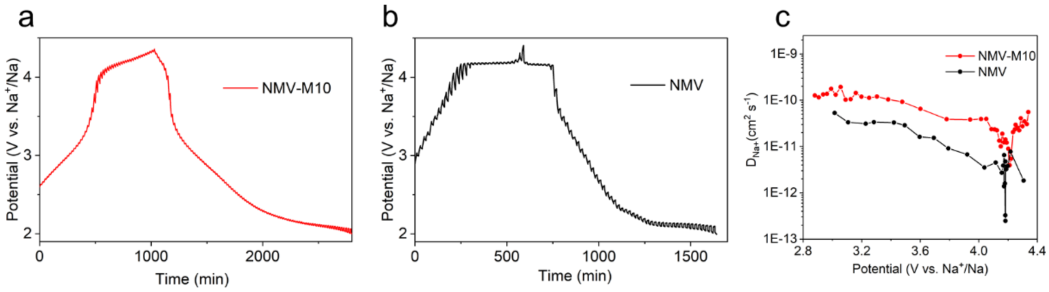

Supplementary Figure 13. GITT tests of (a) NMV-M10 and (b) NMV; (c) the calculated Na^+ diffusion coefficient (D_{Na^+}).

The D_{Na^+} values can be calculated based on the following equation:

$$D_{Na^+} = \frac{4}{\pi\tau}\left(\frac{m_B V_M}{M_B S}\right)^2 \left(\frac{\Delta E_S}{\Delta E_\tau}\right)^2 \quad \left(\tau \ll \frac{L^2}{D_{Na^+}}\right) \qquad \text{S1}$$

Where τ is the pulse duration, m_B and M_B are the active mass and molar mass of NMV or NMV-M10, V_M is the molar volume, and S is the active surface area of the electrode. L is the average radius of the material particles. ΔE_s and ΔE_τ can be obtained from the GITT curves.

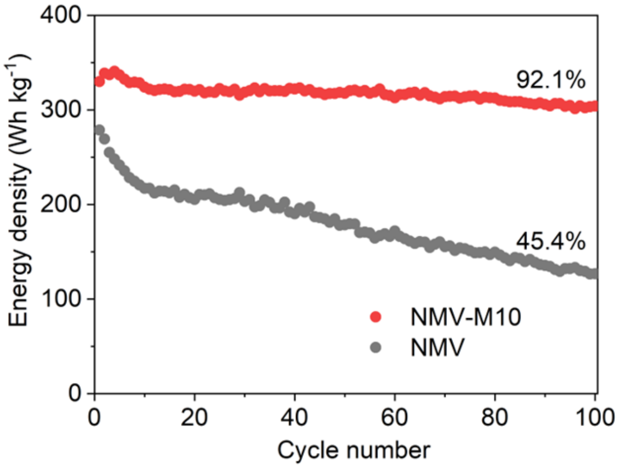

Supplementary Figure 14. Discharge specific energy density comparison of NMV and NMV-M10 at 42 mA g^{-1}. The data of energy densities was exported from the NEWARE battery testing system, which was calculated according to the fomula, $E = \sum(C_s * V_s)$, where E denotes the gravimetric-specific energy density, C_s denotes the instantaneous specific capacity of the cathode material and V_s denotes the instantaneous voltage of the half-cell during discharging process. The total specific energy density is the accumulation of all instantaneous energy densities. The sampling frequency of the device is 10 Hz.

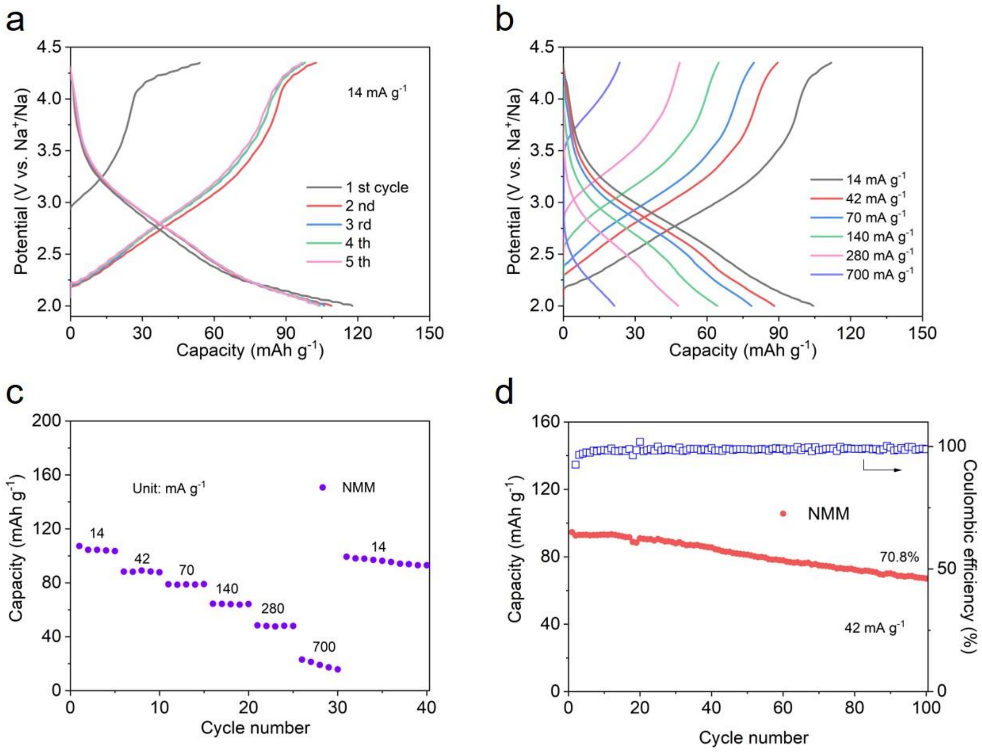

Supplementary Figure 15. Electrochemical performances of NMM. (a) The first five charge/discharge profiles at 14 mA g^{-1}; (b) GCD profiles of the second cycle at different current densities; (c) rate performance; (e) the cycling performance at 42 mA g^{-1}.

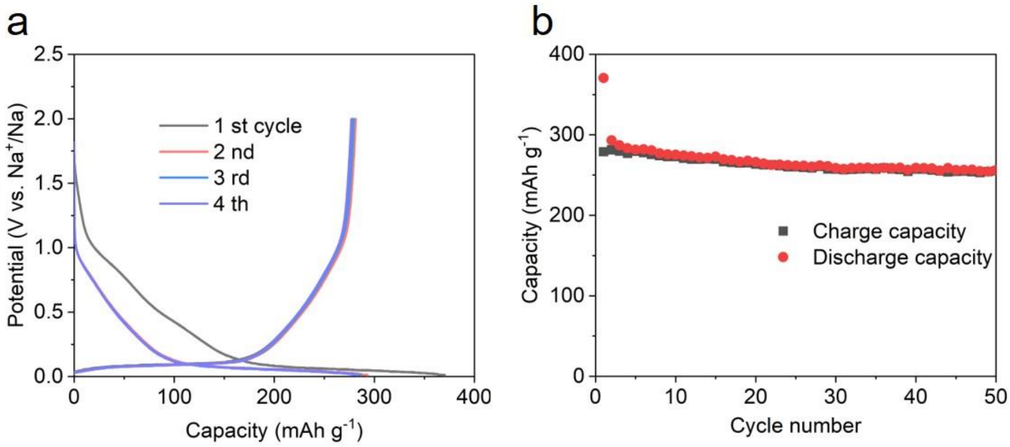

Supplementary Figure 16. Electrochemical performances of the hard carbon. (a) The first four discharge/charge profiles at 50 mA g^{-1} of the commercial hard carbon; (b) the cycling stability at 50 mA g^{-1}.

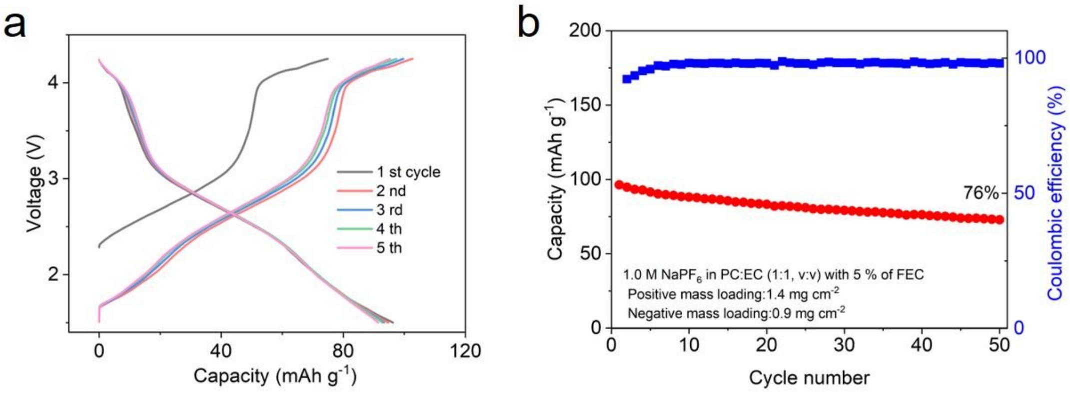

Supplementary Figure 17. Electrochemical performances of the the HC||NMV-M10 full cell. (a) The first five charge/discharge profiles, and (b) the cycling performance of the full cell at the current density of 50 mA g^{-1}. The capacity and tested current is calculated based on the loading of cathode material.

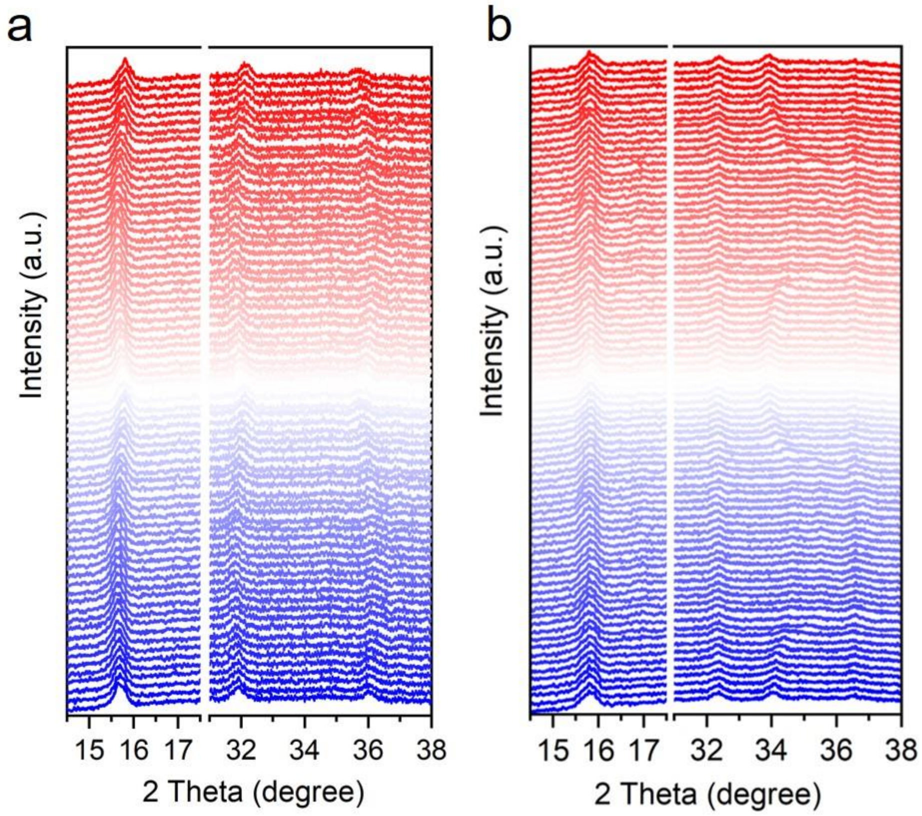

Supplementary Figure 18. In situ XRD patterns of (a) NMV-M10 and (b) NMV during the first two cycles.

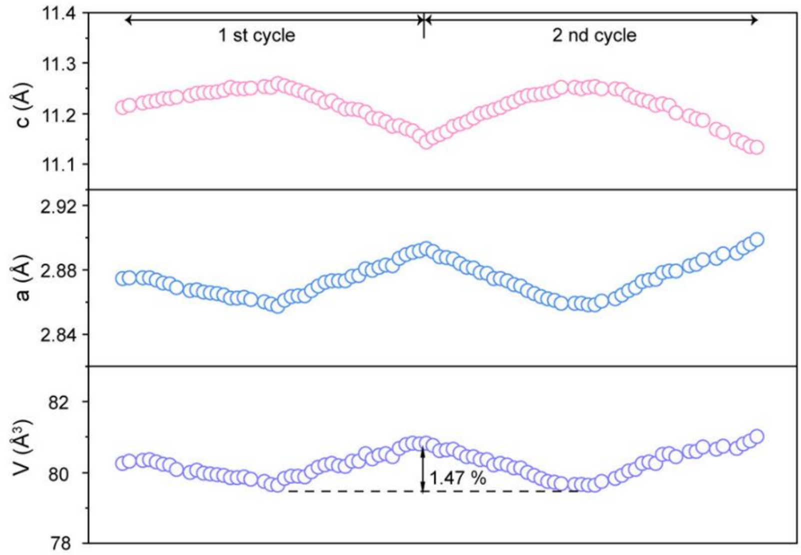

Supplementary Figure 19. The variation of lattice parameters for NMV-M10 during the first two charging/discharging cycles.

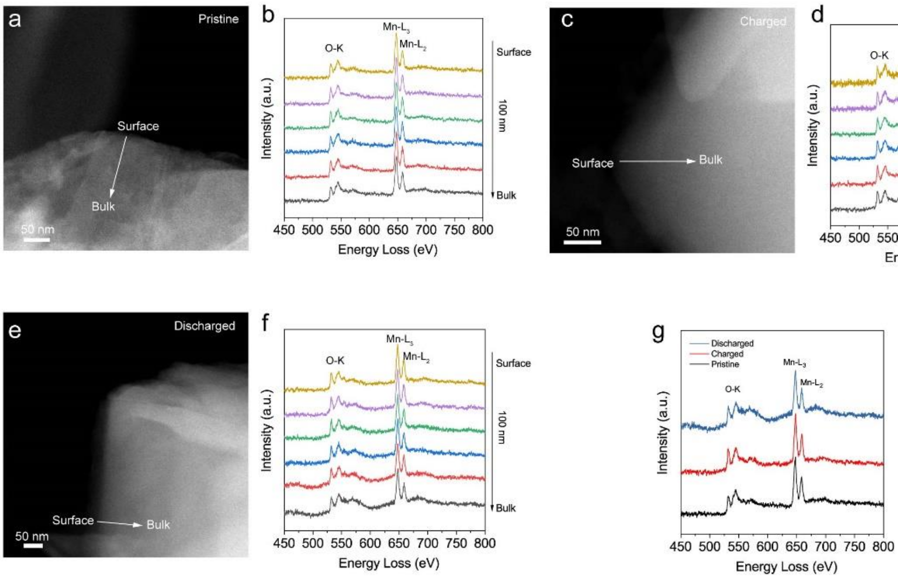

Supplementary Figure 20. The HAADF-STEM images and corresponding ex situ EELS tests scanned from surface to bulk. (a-b) pristine, (c-d) charged to 4.35 V, and (e-f) discharged to 2.0 V. (g) comparison of the EELS results at the charged state from the bulk.

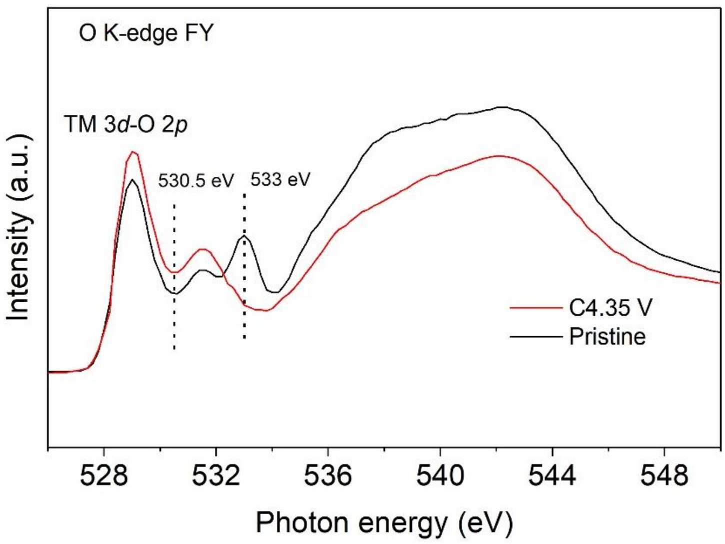

Supplementary Figure 21. Ex situ sXAS of the O-K spectra for NMV-M10.

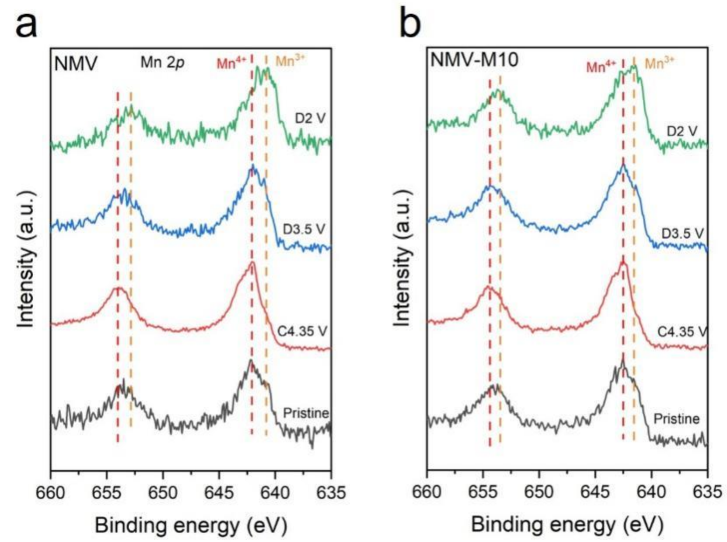

Supplementary Figure 22. Ex situ Mn XPS spectra of (a) NMV and (b) NMV-M10.

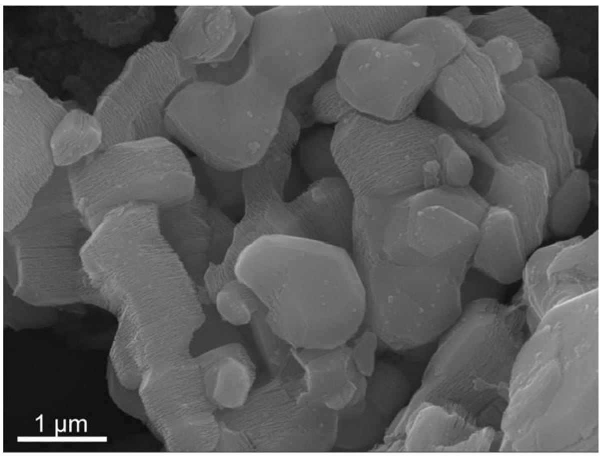

Supplementary Figure 23. Low magnification SEM image of NMV after 100 cycles.

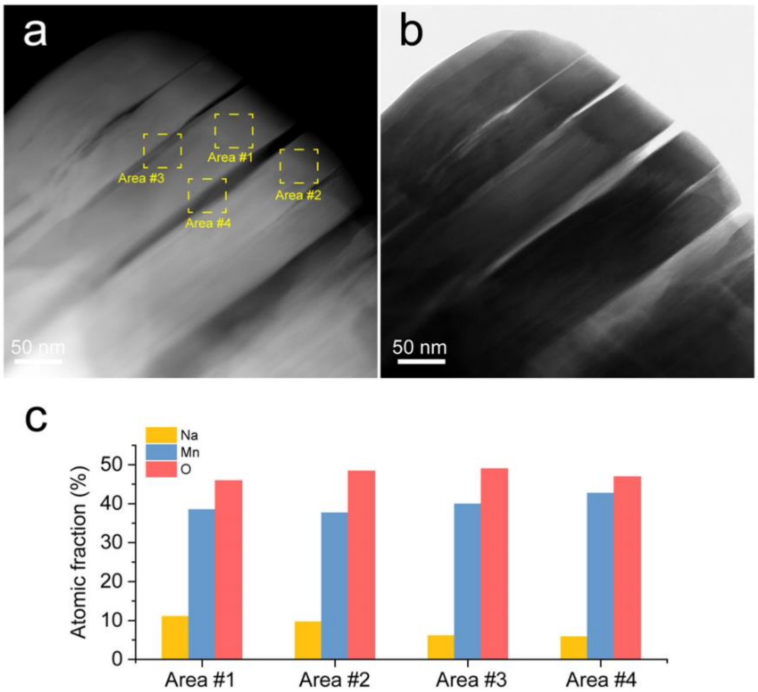

Supplementary Figure 24. (a) HAADF- and (b) ABF-STEM images of the NMV showing cracks; (c) the relative atomic fraction of Na, Mn, O obtained by EDS from different areas, each area was scanned for 10 mins.

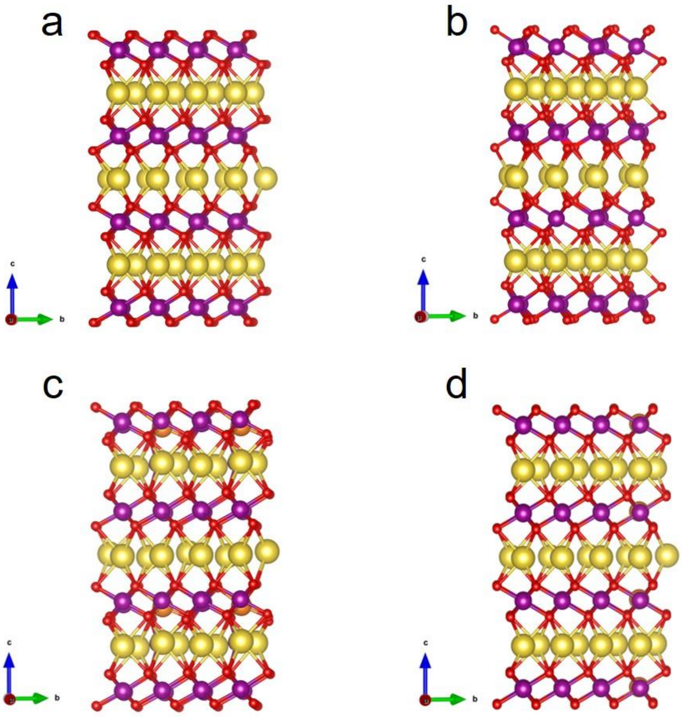

Supplementary Figure 25. The crystal models of (a) $Na_8Mn_{12}O_{24}$ (NM), (b) $Na_8Mn_{11}O_{24}$ (NMV), and (c) $Na_8Mn_{10}MgO_{24}$ (NMV-M), (d) $Na_8Mn_{11}MgO_{24}$ (NMM). Yellow, purple, orange and red balls represent Na, Mn, Mg, and O atoms, respectively. The information of atomic coordinates and occupancy sites are provided in the source data.

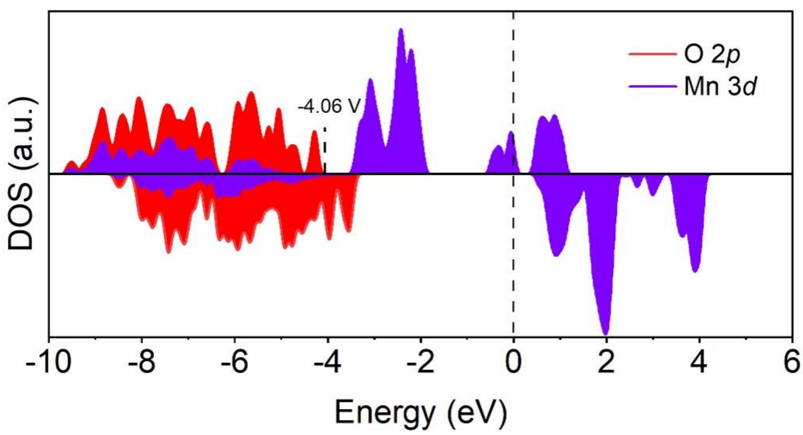

Supplementary Figure 26. The calculated pDOS of NMM.

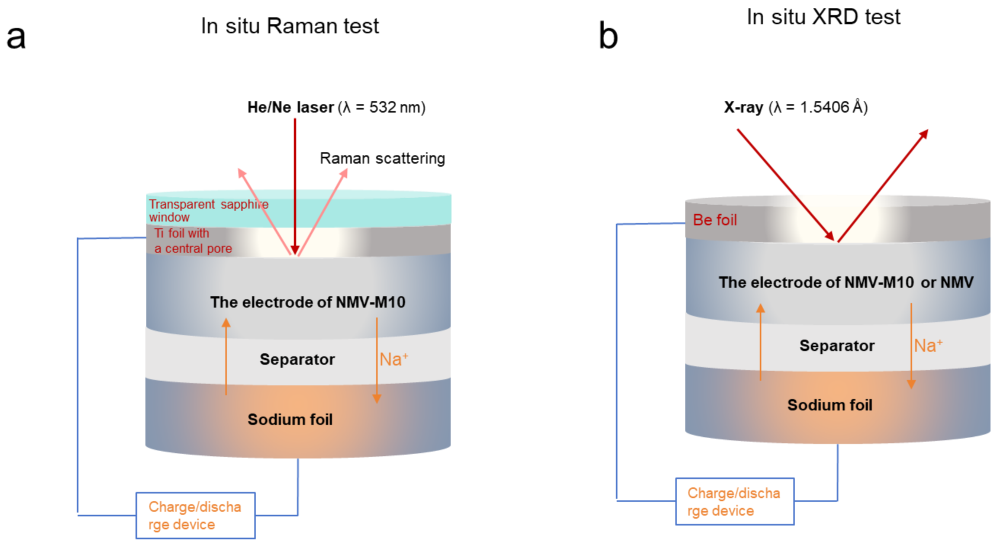

Supplementary Figure 27. Schematic illustration of the devices for (a) in situ Raman and (b) XRD tests.

Supplementary Table 1. Stoichiometry of the NCFMT and NCFMS compounds determined from ICP-OES. The samples were dissolved by aqua regia and measured with the diluted solvent.

Samples	Na : Mg : Mn
NMV	0.685 : 0 : 0.895
NMV-M5	0.670 :0.044:0.866
NMV-M10	0.671 : 0.097 : 0.836
NMV-M15	0.613 : 0.151 : 0.806
NMV-M20	0.684 : 0.197 : 0.798

Supplementary Table 2. Crystallographic parameters of NMV-M10 obtained from XRD Rietveld refinement.

Phase	Atom	Site	*x*	*y*	*z*	Occ	R_{wp}	R_p
P2	Mn1	2a	0	0	0	0.8368	2.12 %	1.65 %
	Mg	2a	0	0	0	0.0997		
	Na_f (1)	2b	0	0	0.25	0.3406(1)		
	Na_e (2)	2d	0.3333	0.6667	0.75	0.2858(1)		
	O	4f	0.3333	0.6667	0.0871(2)	1		
	Mn2	2d	0.3333	0.6667	0.75	0.0110(5)		

$a = b = 2.8704(3)$ Å, $c = 11.2019(1)$ Å, $V = 79.93(1)$ Å^3.

Supplementary Table 3. Crystallographic parameters of NMV obtained from XRD Rietveld refinement.

Phase	Atom	Site	*x*	*y*	*z*	Occ	R_{wp}	R_p
P'2	Mn	4a	0	0	0	0.90	2.61 %	1.88 %
	Na_f (1)	4c	0	0.063(4)	0.25	0.08(6)		
	Na_e (2)	4c	0	0.688(4)	0.25	0.59(6)		
	O	8f	0	0.6523(9)	0.9101(1)	1		
P2	Mn	2a	0	0	0	0.90		
	Na_f (1)	2b	0	0	0.25	0.323(7)		
	Na_e (2)	2d	0.3333	0.6667	0.75	0.347(7)		
	O	4f	0.3333	0.6667	0.0815(5)	1		

P'2 (15.47%): $a = 2.935(3)$ Å, $b = 5.302(5)$ Å, $c = 11.211(3)$ Å, $V = 174.5(3)$ Å^3

P2 (84.13%): $a = b = 2.8674(4)$ Å, $c = 11.149(3)$ Å, $V = 69.4(4)$ Å^3

Supplementary Table 4. The synthesis conditions for different samples. (Unit: mmol)

Samples	**NMV**	**NMV-M5**	**NMV-M10**	**NMV-M15**	**NMV-M20**
Oxalic acid	44	44	44	44	44
$NaNO_3$	7.04	7.04	7.04	7.04	7.04
$Mg(NO_3)_2 \cdot 6H_2O$	0	0.5	1	1.5	2
$Mn(CH_3COO)_2 \cdot 4H_2O$	10	9.5	9	8.5	8

Supplementary Table 5. Electrochemical performance comparison of NMV-M10 and other layered oxide cathodes with anionic redox reaction.

Layered oxide cathode	Anion redox reaction trigged	Voltage range (V)	Measurement condition	References
$Na_2Mn_3O_7$ ($Na_{4/7}Mn_{6/7}\square_{1/7}O_2$)	Vacancy	3-4.65	50 cycles at 0.1C 76.4%	[1]
$Na_{0.653}Mn_{0.929}\square_{0.071}O_2$	Vacancy	1.5-4.3	60 cycles at 0.1 C 86.7%	[2]
$Na_{2/3}Mg_{1/3}Mn_{2/3}O_2$	Mg	2-4.5	100 cycles at 1 C 80%	[3]
$Na_{2/3}Mn_{0.72}Cu_{0.22}Mg_{0.06}O_2$	Mg	2-4.5	100 cycles at 1 C 87.9%	[4]
$Na_{2/3}[Mn_{7/9}Zn_{2/9}]O_2$	Zn	1.5-4.5	50 cycles at 0.1 C 60%	[5]
$NaLi_{1/9}Ni_{2/9}Fe_{2/9}Mn_{4/9}O_2$	Li	2-4.3	200 cycles at 1 C 82.8%	[6]
This work	**Mg, vacancy**	**2-4.35**	**200 cycles at 1 C (140 mA g^{-1}) 87.5%**	

Supplementary References

1. Song, B. *et al.* Understanding the Low-Voltage Hysteresis of Anionic Redox in $Na_2Mn_3O_7$. *Chem. Mater.* **31**, 3756-3765 (2019).
2. Zhao, C., Wang, Q., Lu, Y., Jiang, L., Liu, L., Yu, X., Chen, L., Li, B., Hu, Y.-S. Decreasing Transition Metal Triggered Oxygen Redox Activity in Na-Deficient Oxides. *Energy Storage Mater.* **20**, 395-400 (2019).
3. Dai, K. *et al.* High Reversibility of Lattice Oxygen Redox Quantified by Direct Bulk Probes of Both Anionic and Cationic Redox Reactions. *Joule* **3**, 518-541 (2019).
4. Wang, P.-F. *et al.* Both Cationic and Anionic Redox Chemistry in a P2-Type Sodium Layered Oxide *Nano Energy*, **69**, 104474 (2020).
5. Bai, X. *et al.* Anionic Redox Activity in a Newly Zn-Doped Sodium Layered Oxide P2-$Na_{2/3}Mn_{1-y}Zn_yO_2$ ($0 < y < 0.23$). *Adv. Energy Mater.* **8** (32), 1802379 (2018).
6. Guo, Y. *et al.* Boron-Doped Sodium Layered Oxide for Reversible Oxygen Redox Reaction in Na-ion Battery Cathodes. *Nat. Commun.* **12**, 5267 (2021)